ADVANCED FUNCTIONAL MATERIALS
www.afm-journal.de

Assembly and Characterizations of Bifunctional Fluorescent and Magnetic Microneedles With One Decade Length Tunability

*Jean-Baptiste Lugagne, Gwennhaël Brackx, Emek Seyrek, Sophie Nowak, Yann Sivry, Leticia Vitorazi, Jean-François Berret, Pascal Hersen, and Gaëlle Charron**

This report presents the fabrication of bifunctional magnetic and fluorescent microneedles (μNDs) made of a ternary mixture of magnetic nanoparticles (NPs), quantum dots (QDs), and polyelectrolyte. The assembly relies on the electrostatic complexation of negatively charged NPs with positively charged polymer strands and is controlled by the charge ratio between the nanoparticle building blocks and the polymer mortar. The resulting 1D objects can be actuated using an external magnetic field and can be imaged using fluorescence microscopy, thanks to the fluorescent and superparamagnetic properties inherited from their NP constituents. Using a combination of core and surface characterizations and a state-of-the-art image analysis algorithm, the dependence of the brightness and length on the ternary composition is thoroughly investigated. In particular, statistics on hundreds of μNDs with a range of compositions show that the μNDs have a log-lormal length distribution and that their mean length can be robustly tuned in the 5–50 μm range to match the relevant length scales of various applications in micromixing, bioassays or biomechanics.

1. Introduction

1D-magnetic microstructures made of single magnetic microparticles or assemblies of magnetic nanoparticles (mNPs) can find applications in a wide variety of fields that includes composite materials, microfluidics, and micromechanics. Microrods of nonmagnetic material coated with iron oxide nanoparticles have been used to mechanically reinforce polymer matrices through applying small magnetic fields.[1] Micromachined pieces of magnetic materials or chains of magnetic colloids have been applied as microstir bars to increase the efficiency of mixing in microfluidic channels and microdroplets.[2–6] Mixing at the microscale can also be enhanced using micropillars or artificial cilia consisting of magnetic micro or nanoparticle assemblies that can be actuated through application of a rotating or a swinging magnetic field.[7] These magnetic cilia can form the basis of flow or vibration sensing when coupled to a giant magnetoresistive sensing element that monitors their deflection.[8,9] Alternatively, the bending of these cilia under a static external field can serve as a mean to apply controlled stresses to soft materials deposited on the substrate such as tissues, films or cells in order to study their mechanical responses.[10–12] In the same line, free standing magnetic microrods can be used as active microrheometers to probe the viscoelastic properties of complex fluids, including living cells, with microscale resolution.[13,14]

Many of these applications would benefit from the addition of a fluorescent functionality to the magnetic one. Incorporating fluorophores into the 1D-microstructures enables easier imaging in scattering media. It could allow for optical bar-coding of the magnetic microactuators. In cell mechanics studies, it could give insights into the environment of the magnetic probe through colocalization experiments involving organelle-specific fluorophores. Moreover, most of these applications simultaneously require the length of the 1D-magnetic microstructures to be adjusted to the problem at play. Microstirrers need to be attuned to the dimensions of the fluid compartment and to its viscosity. The range of forces to which magnetic microposts are sensitive depends on their length and thickness. To be able to resolve inhomogeneities in viscoelastic properties at the microscale, magnetic microrheometers need to be of dimensions comparable to the typical length scale of the structural inhomogeneities.[15,16]

Bifunctional magnetic and fluorescent nano- or microspheres have been reported in the past. They were developed

Dr. J.-B. Lugagne, Dr. G. Brackx, Dr. E. Seyrek, Dr. L. Vitorazi, Dr. J.-F. Berret, Dr. P. Hersen, Dr. G. Charron
Laboratoire Matière et Systèmes Complexes
UMR 7057
Université Paris Diderot
Sorbonne Paris Cité
CNRS
10 rue Alice Domon et Léonie Duquet, 75205 Paris cedex 13, France
E-mail: gaelle.charron@univ-paris-diderot.fr
Dr. S. Nowak
X-Ray Platform
Chemistry Department
Université Paris Diderot
Sorbonne Paris Cité
35 rue Hélène Brion, 75205 Paris cedex 13, France
Dr. Y. Sivry
Institut de Géophysique du Globe de Paris
UMR 7154
Université Paris Diderot
Sorbonne Paris Cité
CNRS
1 rue Jussieu, 75005 Paris, France

DOI: 10.1002/adfm.201700362

mostly toward applications in bimodal magnetic resonance and fluorescence imaging, drug delivery, or bioassays. These materials have been synthesized according to various strategies: core–shell particles, where a core of magnetic material (e.g., iron oxide nanoparticles) is encased in a shell of fluorescent one (e.g., dye-labeled silica or quantum dots) or the other way round;[17–19] raspberry-like particles, where large particles of one material are decorated on their surface with smaller particles of the other material;[20,21] colloidosomes self-assembled from fluorescent and magnetic colloids;[22] beads in which particles of both materials have been coprecipitated or coembedded in a silica or polymer matrix;[23–25] and particles made of oxides of rare earth ions.[26] Most of these strategies lead to bifunctional spheres in the 0.1–1 μm range whose size cannot be easily tuned. In general, they are not amenable to synthesize 1D structures. Moreover, in many cases the synthetic cost is high, either because of the minute scale of production or because of the time or number of steps required. We report here on the fabrication of bifunctional magnetic and fluorescent 1D-structures of micrometric length assembled by controlled aggregation of a ternary mixture of polyelectrolyte, superparamagnetic nanoparticles and quantum dots. The building blocks are simple and easily sourced. Assembly proceeds in water, in less than half an hour, to give rise to wire or needle-like aggregates of millions of nanoparticles that are responsive under an external magnetic field and can be imaged by conventional epifluorescence microscopy. Interestingly, by playing on the ternary composition, their mean length can be tuned in the 5–50 μm range to match the needs of many microfluidic or biophysical applications. As an illustration of the potential of the microneedles (μNDs) for cell mechanics studies, we show that they can be internalized by HeLa cells and that their fluorescence can be used to assess their localization with regards to cellular compartments.

2. Results and Discussion

2.1. General Strategy for Assembling Fluorescent and Magnetic Microneedles

2.1.1. Assembly of First-Generation μNDs

The bifunctional magnetic μNDs derive from a first generation of magnetic-only 1D-microstructures reported previously. This first generation of magnetic μNDs was obtained by electrostatic complexation of negatively charged mNPs with polycationic polymers in a kinetically controlled fashion.[27–29] The magnetic building blocks consisted of 6–8 nm superparamagnetic Fe_2O_3 maghemite NPs coated in a 3 nm thick layer of sodium polyacrylate that imparted them a persistent colloidal stability, even at high ionic strength (≥1 M). Various polyelectrolytes bearing positive charges through ammoniums (either quaternary or proton-exchanging) were investigated and all led to successful assembly.[30]

Due to the strong driving force for electrostatic assembly, direct mixing of the NP building blocks and polyelectrolyte glue resulted in macroscopic precipitation of large aggregates. The assembly protocol was therefore designed to slow down the interaction. To this end, the constituents were mixed in the presence of a screening electrolyte at high ionic strength (typically in the M range), at which stage they remained individually dispersed. Assembly was then driven by slow dialysis of the screening electrolyte to give rise to spherical clusters when the ionic strength decreased below a threshold value. When performing the assembly under a static magnetic field (typically of 0.3 T), 1D structures grew and led to microneedles between 150 and 400 nm in width and 1 and 500 μm in length that displayed superparamagnetism inherited from their iron oxide constituents. Starting binary compositions were referenced using the charge ratio Z, defined as the number of negative charges brought by the mNPs divided by the number of positive charges brought by the polymer (Equation (1))

$$Z = \frac{C^{\ominus}_{\mathrm{mNP}} V_{\mathrm{mNP}}}{C^{\oplus}_{\mathrm{pol}} V_{\mathrm{pol}}} \tag{1}$$

where $C^{\ominus}_{\mathrm{mNP}}, V_{\mathrm{mNP}}, C^{\oplus}_{\mathrm{pol}}$, and V_{pol} are the concentration of negative surface charges borne by the mNPs in the mNP stock solution, the volume of mNP stock solution, the concentration of positive charges borne by the polymer in the polymer stock solution and the volume of polymer stock solution respectively.

2.1.2. Choice of Constituents for Fluorescent Magnetic μNDs

One possible strategy to incorporate a fluorescent functionality into the magnetic μNDs described above consists in substituting fluorescent building blocks for a fraction of the magnetic ones. Fluorescent NPs then need to present the same chemical reactivity as mNPs with regards to the assembly mechanism. This implies that they must bear negative charges on their surface and, critically, display colloidal stability even at high ionic strength. With the aim of tracking the μNDs using fluorescence (video) microscopy, the μNDs should ideally be as bright as possible. Indeed, strong brightness not only increases contrast but also enables the use of short exposure times and therefore gives access to shorter timescales of dynamic tracking. Moreover, the μNDs should display homogeneous fluorescence, namely should be homogeneously doped with fluorescent blocks, so that the fluorescence profile tightly mirrors the shape of the object. In a solid state solution, doping is facilitated by a similarity of size between the dopant and the host. Based on the same principle, the fluorescent building blocks and the magnetic ones should have diameters of the same order of magnitude. Taking into account these criteria, we selected the $AgInS_2$–ZnS (ZAIS) quantum dots (QDs) described by Regulacio et al. as fluorescent building blocks (**Figure 1**).[31] These hydrosoluble QDs were synthesized directly in water and were a few nm in diameter. Their emission was composition-dependent and could be tuned from 525 to 640 nm, with a maximum reported quantum yield of 20%. Interestingly, these QDs were synthesized in the presence of polyacrylic acid (PAA), which acted as a capping agent. Having a diameter within the same range as the mNPs and the exact same coating, we expected these QDs to be an ideal dopant for the μNDs.

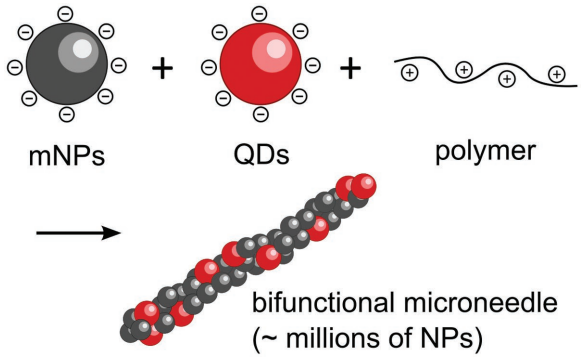

Figure 1. Synthetic scheme for assembly of bifunctional fluorescent magnetic microneedles (μNDs) from a ternary mixture of magnetic nanoparticles (mNPs), quantum dots (QDs), and polymer.

2.1.3. Characterizations of Magnetic and Fluorescent Building Blocks for μND Assembly

The mNPs used for μND assembly were synthesized following the Massart method and coated in a post-synthetic fashion with PAA, as described earlier.[32,33] The detailed characterizations of the exact batch used in this study are presented in the Supporting Information. Hereafter, we present the characterizations of the QDs we synthesized using the procedure from Regulacio et al. with few modifications, and compare the QD characteristics to those of the mNPs used for μND assembly (**Table 1**).[31]

Optical Properties: Iron oxide NPs present an intense and continuous absorption in the UV-vis range that vanishes close to 610 nm. We therefore aimed at synthesizing orange to red-emitting QDs to prevent fluorescence quenching through energy transfer to or reabsorption by the host matrix of the μND. The synthesized QDs had a maximum emission peak centered at 600 nm and a moderate quantum yield of 7%, which was compensated by the emission sitting well outside the iron oxide absorption range (Figure S1; experimental details regarding the determination of the quantum yield are provided in the Supporting Information).

According to Inductively Coupled Plasma Optical Emission Spectrometry (ICP-OES) analysis, the QDs had a nonstoichiometric $Ag_{0.23}In_{0.58}Zn_{1.54}S_3$ formula, reflecting an excess chalcogen compared to the metal ions and a defect in silver compared to indium, which is consistent with orange emission (Table S3, Supporting Information).[34]

Size Properties: TEM images of QDs reveal a 5.8 ± 1.2 nm core diameter based on counting 175 NPs (Figure S5, Supporting Information). The hydrodynamic diameter as determined by Dynamic Light Scattering (DLS) was 13 nm in pure water at pH 8.5 (Figure S6, Supporting Information). The QDs and mNPs therefore had dimensions of the same order of magnitude, both regarding their inorganic core and their size in solution. Importantly, the hydrodynamic diameter of QDs remained unchanged in the screening electrolyte solution used for μND assembly (1 M NH_4Cl/NH_4OH) over a period of days, evidencing remarkable colloidal stability due to the PAA coating. Just as the mNPs, the QDs were resilient toward the μND assembly conditions.

Charge Density and Concentration: As evidenced by gel electrophoresis on agarose and consistently with PAA coating, the QDs were negatively charged (Figure S10, Supporting Information). They also exhibited a higher number of surface carboxylates per core mass unit than the mNPs, a fact that was confirmed by analysis of the composition of both batches of QDs and mNPs, by ICP-OES for the inorganic core elemental concentrations and pH-titration for the surface carboxylates (see the Supporting Information).[35] Detailed compositions of the stock solutions are provided in Tables S4 and S5 (Supporting Information).

Table 1. Summary of QD and mNP physicochemical characteristics: inorganic core diameter (D_c), hydrodynamic diameter (D_H), inorganic core composition, nature of the organic coating and surface charge density (in moles of ionizable surface groups per g of inorganic core material).

NPs	D_c [nm]	D_H [nm]	Core composition	Coating composition	Charge density [mmol g^{-1}]
QDs	5.8 ± 1.2	≈13	$Ag_{0.23}In_{0.58}Zn_{1.54}S_3$	PAA	3.865 ± 0.242
mNPs	9.4 ± 1.7	≈31	Fe_2O_3	PAA	0.975 ± 0.262

2.2. Assembly of Fluorescent Magnetic Microneedles

Assembly, of fluorescent magnetic μNDs was performed following the same synthetic procedure as those developed previously for magnetic-only μNDs, but for the substitution of QDs for a fraction w of mNPs (Equation (2)).

For a given assembly procedure, the starting reagent stoichiometry is unambiguously defined by two synthetic parameters: w and the previously defined Z ratio between negative charges brought by the nanoparticles and positive charges brought by the polymer, which now takes into account the contribution of QDs (Equation (3)).

$$w = \frac{V_{QD}}{V_{mNP} + V_{QD}} \tag{2}$$

$$Z = \frac{C^{\ominus}_{mNP} V_{mNP} + C^{\ominus}_{QD} V_{QD}}{C^{\oplus}_{pol} V_{pol}} \tag{3}$$

where V_{QD} and $C^{\ominus}_{QD}$ are the volume of the QD stock solution and the concentration of negative charges borne by the QDs in the QD stock solution.

Alternatively, the ternary composition can be depicted using the molar fractions of the charges respectively brought by QDs, mNPs, and polymer, according to Equations (4).

$$x_{QD} = \frac{C^{\ominus}_{QD}}{C^{\ominus}_{QD} + C^{\ominus}_{mNP} + C^{\oplus}_{pol}}$$
$$x_{mNP} = \frac{C^{\ominus}_{mNP}}{C^{\ominus}_{QD} + C^{\ominus}_{mNP} + C^{\oplus}_{pol}} \tag{4}$$
$$x_{pol} = \frac{C^{\oplus}_{pol}}{C^{\ominus}_{QD} + C^{\ominus}_{mNP} + C^{\oplus}_{pol}}$$

A set of 15 {Z; w} compositions with $Z \in [0.62 - 7.01]$ and $w \in [0.00 - 0.20]$ was investigated (Table S6, Supporting

Information). The individually dispersed mNPs are too small to be collected using a table magnet but their aggregates have a much higher saturation magnetization. Successful decantation under an applied magnetic field (typically of 10–100 mT) therefore evidences that assembly has taken place. According to this indicator, we observed that all investigated compositions successfully led to µND assembly. TEM imaging confirmed that the aggregates are made of densely packed nanoparticles (Figure S12, Supporting Information).

2.3. Properties of QD-Doped Magnetic µNDs

2.3.1. Overview of Properties: Fluorescence and Responsiveness under Magnetic Actuation

Figure 2a depicts a phase 20X contrast image of the aggregates obtained starting from the {Z = 3.62; w = 0.15} composition. Straight µNDs are obtained with lengths widely distributed between about 5 and 50 µm and diameters of about 0.3–1.0 µm. Their morphology is identical to the magnetic-only µNDs reported previously. Figure 2b displays the same specimen area imaged by epifluorescence microscopy. The µNDs emit in the red range under green excitation and appear homogeneously bright, evidencing homogeneous incorporation of the QDs in the host µND matrix and retention of their optical properties. When depositing a soft permanent magnet on the microscope stage, the µNDs respond to the external magnetic actuation by aligning along the field lines (Figure 2c,d). Upon suppressing the external magnetic field, the µNDs relax toward randomized orientations, thereby evidencing that the bifunctional µNDs retain the superparamagnetic behavior of the magnetic-only objects they are derived from.[13,14]

Interestingly, the morphology and in particular the length of the µNDs vary with the starting composition (**Figure 3**). While {Z = 4.20; w = 0.20} µNDs have a length comprised between about 5 and 50 µm, {Z = 1.40; w = 0.20} µNDs which have the same QDs substitution ratio range from 6 to 220 µm. Both samples display straight persistent needle-like aggregates. In contrast, the {Z = 1.21; w = 0.15} sample contains large, soft, hair strand-like bundles of µNDs, along with some individual µNDs. In addition, the longer the µNDs or bundles of µNDs, the brighter they are (due to their being thicker). As both the length of the µNDs and their brightness ultimately determine their potential application, a systematic investigation of these parameters as a function of ternary composition was conducted.

2.3.2. Systematic Investigation of Length and Brightness as a Function of Ternary Composition

Tools for Image Analysis: The distribution of length was analyzed from phase contrast microscopy images acquired with 10X, 20X, and 40X objectives. Lengths were extracted using an in-house,

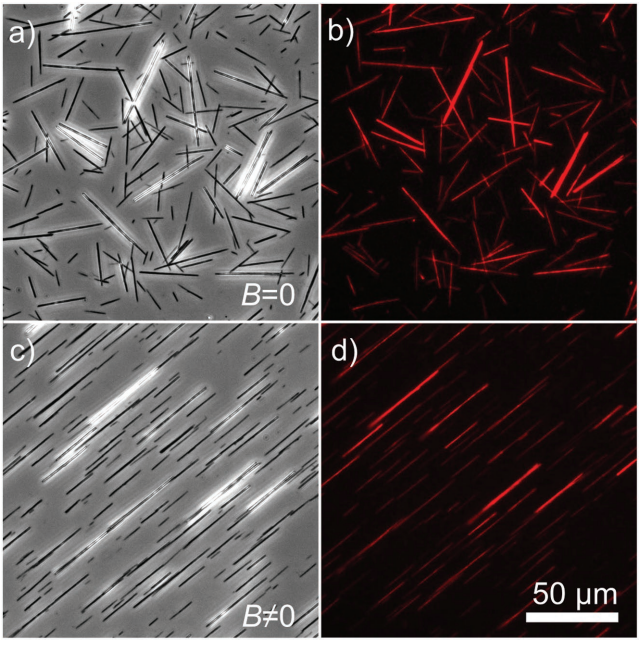

Figure 2. a,c) Phase contrast and b,d) epifluorescence microscopy images of µNDs having the composition {Z = 3.62; w = 0.15}, a,b) without and c,d) under static magnetic field. Z is the ratio of negative to positive charges while w is the substituting ratio of QDs for mNPs, as defined in Equations (2) and (3).

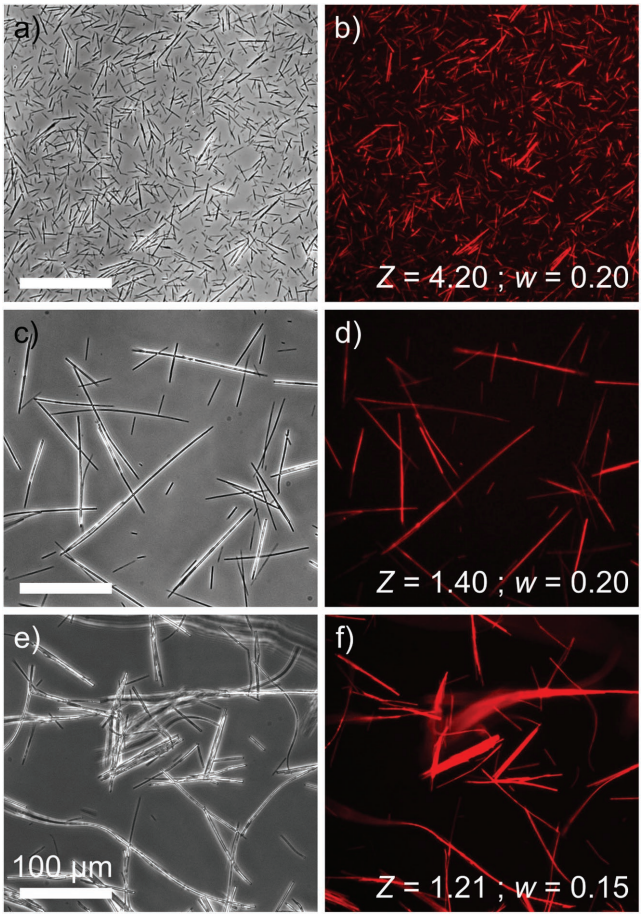

Figure 3. a,c,e) Phase contrast and b,d,f) epifluorescence microscopy images of bifunctional µNDs having various compositions.

dedicated image analysis Matlab code (available at http://lab513.github.io/Houghneedles/). The algorithm for μND recognition was based on the linear Hough transform, which is a feature extraction technique devoted to the identification of lines.[36] The software is successful in recognizing single objects in an entangled bunch of μNDs but not when the μNDs are bundled (**Figure 4**). It is biased against smaller μNDs due to their comparatively lower contrast. The software features a graphical user interface for quick and handy correction of the most obvious errors, such as μNDs identified shorter than they are due to uneven contrast along their length or wires aligned tip-to-tip mistaken for one long object. Using this automated image analysis tool, 750 μNDs on average were counted per sample comprising individual μNDs, with no less than 200 μNDs counted for that having the highest mean length. Note that when individual μNDs coexisted with hair strand-like bundles (as in Figure 3e), only the individual and straight needle-like objects were counted. All length distributions were log-normal with relative standard deviations ranging from 15% to 23% (Figure 4, and Figures S13 and S14, Supporting Information).

Fluorescence analysis was performed based on epifluorescence microscopy images acquired with a single 20X objective. The brightness of each sample was taken as the mean background-corrected intensity of the identified bright pixels in the set of sample images (Figures S15 and S16, Supporting Information). The dependencies of brightness and mean length on ternary composition are depicted in **Figure 5** (see also Table S7 and Figure S17, Supporting Information).

Tuning of Brightness: We investigated the efficiency of QD incorporation by looking at the relative brightnesses of μNDs

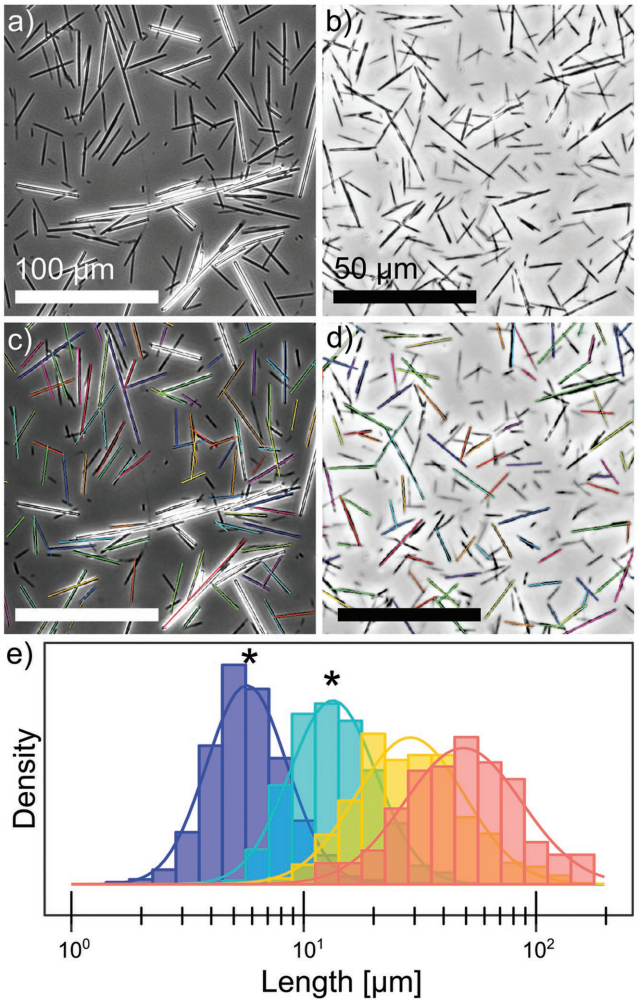

Figure 4. Examples of μND length determination using the linear Hough transform-based software. a,b) Original phase contrast images and c,d) phase contrast images displaying μNDs identified by the software for compositions $\{Z = 3.03; w = 0.1\}$ and $\{Z = 4.20; w = 0.2\}$, respectively. e) Examples of length distributions obtained across the ternary composition range and estimated by counting 750 objects on average from three images for each sample. Asterisks indicate the length distributions of the two afore-mentioned samples. The length distributions of all compositions are summarized in Figures S13–S15 (Supporting Information).

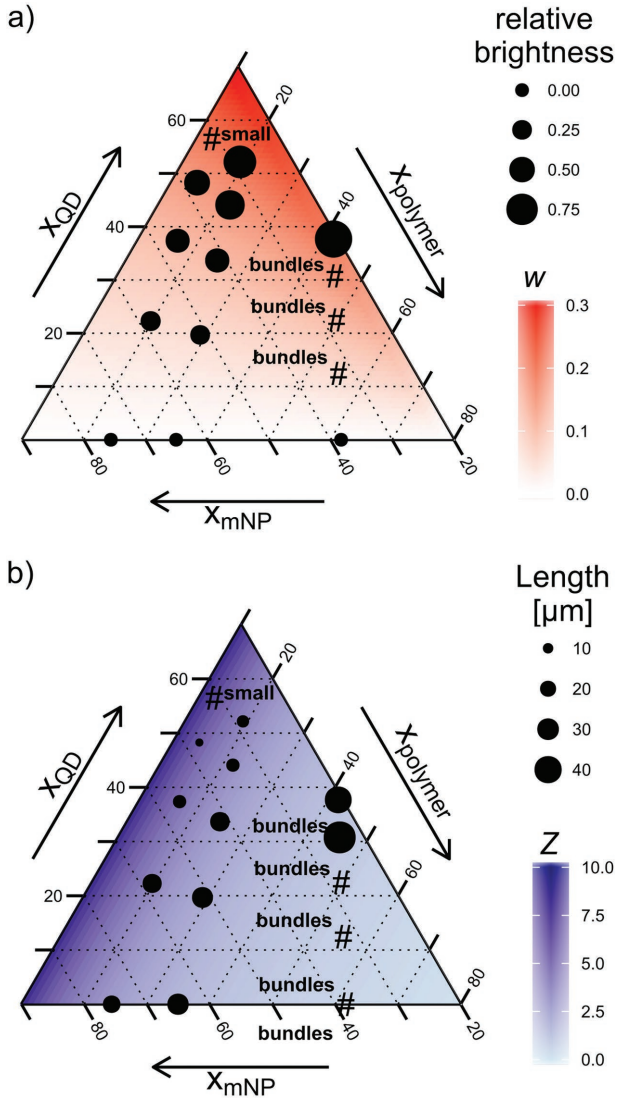

Figure 5. a) Relative fluorescence brightness and b) geometric mean length as a function of $\{x_{mNP}, x_{QD}, x_{pol}\}$ ternary molar composition, as defined in Equation (4). Hash symbols indicate ternary compositions for which the geometric mean length or brightness could not be extracted using our imaging setup, the μNDs being too small or aggregated as bundles.

across the range of investigated compositions (Figure 5a). As a general trend, starting compositions richer in QDs display higher relative brightness. This observation evidences that the actual incorporation ratio parallels the starting doping ratio and supports the hypothesized similarity in reactivity between PAA-coated QDs and PAA-coated mNPs. The nonmagnetic QDs are not segregated during the magnetic field-driven assembly process. Hence, to increase the fluorescence brightness of the μNDs, one simply needs to enrich the molar fraction of QDs of the starting ternary mixture.

Tuning of Length: Out of the 15 investigated compositions, our imaging setup allowed for the estimation of the length distribution of 11 samples (Figure 5b). Each of those distributions had a log-normal profile, consistently with what has previously been observed for supracolloidal aggregates and colloidosomes (Figure 4e, and Figures S13–S15, Supporting Information).[37–41] Mapping the Z ratio over the ternary diagram reveals that the length decreases with increasing Z, with the geometric mean length ranging from 5.7 to 48.5 μm for $Z = 6.03$ to 1.21 respectively. Three compositions led to large bundles of aggregated μNDs whose length could not be extracted; they corresponded to the weakest Z ratios across the whole range of molar fractions ($Z = 0.62$, 0.82, and 1.01 respectively). For the sample corresponding to the highest Z value (7.01), the μNDs could not be resolved using the 40X objective, although assembly had indeed taken place since the product could be magnetically decanted with a table magnet, albeit admittedly very slowly, and since TEM images displayed aggregates (Figure S15, Supporting Information). The dependence of the mean length on the composition was rationalized earlier for magnetic-only μNDs.[28] The assembly of μNDs was shown to occur in two steps that are not separated in time. In a first nucleation step, supracolloidal clusters are formed due to the electrostatic complexation between negatively charged mNPs and positively charged polymer strands once the ionic strength falls below a certain threshold. In a second growth step, clusters align along the magnetic field lines, assemble and then fuse due to magnetic dipolar attraction (Figure S19, Supporting Information). The surface charge of the clusters was found to mirror the Z ratio of the starting mixture, with compositions featuring excess mNPs ($Z > 1$) leading to negatively charged clusters and those featuring an excess polycation ($Z < 1$) leading to positively charged ones.[30] The kinetics of assembly therefore results from the balance between dipolar magnetic attraction and electrostatic repulsion between the supracolloidal clusters. At Z ratio close to 1, the clusters bear a weak net charge and therefore, their mutual electrostatic repulsion is weak and quickly overcome by the dipolar magnetic attraction during the dialysis process. On the contrary, when the Z ratio is high, intermediate clusters bear a stronger net negative charge. They repel each other more efficiently and the electrostatic repulsion is not so largely compensated by the dipolar magnetic attraction. Weak Z ratios are thus expected to lead to thick and long microneedles, while high Z ratios are expected to give rise to much shorter microneedles.[30]

We attempted at modelling the dependency of the length on compositional parameters in the case of the bifunctional μNDs. The dependence of the length on the Z ratio in fluorescent magnetic μNDs appears fully consistent with the afore-mentioned mechanism. There is strong anticorrelation at the 95% confidence level between length and Z ratio (see the Supporting Information for details of the *t*-test). The shortest μNDs correspond to compositions having the largest Z absolute values due to the increased electrostatic repulsion between clusters. As the QD building blocks have a higher surface charge density than the mNPs, these shortest μNDs are also the richest in QDs. Since ZAIS QDs are diamagnetic, their incorporation should lessen the saturation magnetization of the clusters. For a given Z value, a higher QD doping ratio should therefore lead to less intense magnetic dipolar attraction between clusters. One might expect this phenomenon to slow down the assembly and lower the length of the resulting μNDs. However, a t-test conducted on the data indicated no significant correlation between the length and the doping ratio w (see the Supporting Information). Finally, the dependency of the length on the compositional parameters could be simply described as Equation (5) (**Figure 6**).

$$L \simeq 65 \times \exp(-0.33Z) \tag{5}$$

where L is the geometric mean length and Z varies in the 1.2–6.0 range (Akaike information criterion was applied to choose the best model, see the Supporting Information).

Because of their length tunability in the 5–50 μm range and the ease with which they can be assembled, the bifunctional fluorescent magnetic μNDs could find applications in multiple domains. Microfluidic channels have a typical width of 5–200 μm. At the upper end of this size window, 30–50 μm μNDs could be used as individual microstir bars as a cheaper alternative to micromachined devices that have been reported earlier.[5] Shorter μNDs could be easily incorporated as multiple stir bars in arrays of microdroplets to efficiently churn up the whole solution compartments.[3,4] The magnetic actuation and fluorescent features could be exploited in simultaneous

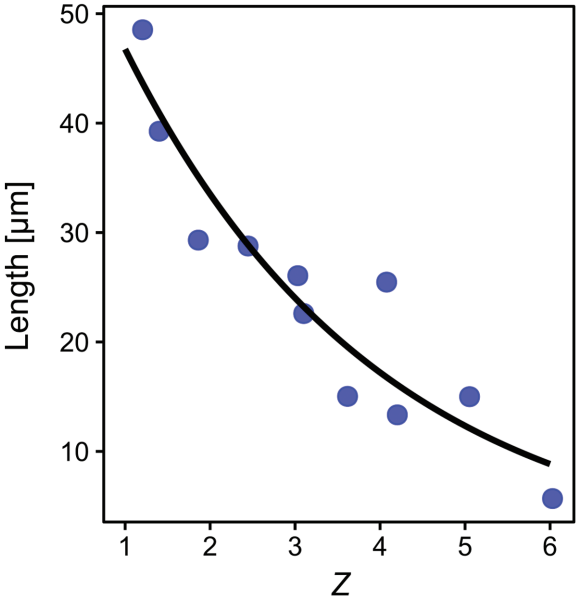

Figure 6. Geometric mean length of μNDs as a function of Z (blue dots) and best-fit line according to Equation (5) (black line).

magnetic and fluorescence-assisted cell sorting.[42] Alternatively, the bifunctional μNDs could act as probes for active viscosimetry-based label-free bioassays.[43] In both of these assaying applications, the synthetic control over the length would enable fine tuning the probe to the application through optimizing the saturation magnetization of the μNDs. Finally, μNDs could allow to probe the mechanical properties of biological materials such as tissues, films, individual cells or subcellular compartments using magnetic actuation-based techniques coupled to fluorescence imaging. Lately, the viscoelastic properties of cells and tissues have attracted much attention in the frame of medical research. For instance, the mechanical stiffness of cancer cells has been shown to correlate with their metastatic potential, with softer more deformable cells having the highest migratory potential and invasiveness.[44] Moreover, a cell state or fate can be controlled by the viscoelastic properties of its environment.[45] The phenomena at play are difficult to study by conventional macroscopic rheological methods since the samples typically come as tiny specimens and biological fluids are generally complex, i.e., they behave differently at different length scales. In this context, the size tunability over the 5–50 μm range is especially appealing since it would enable the study of a given material from the scale of assemblies of cells down to the subcellular level with a single technique suited to microscopic specimens.[16] Such multiscale study would shine light on the respective contributions and interplay of the mechanics of cells, organites, and surrounding matrix.[15]

2.4. Intracellular Imaging of Fluorescent Magnetic Microneedles

Since many of these applications would rely on interaction of the bifunctional μNDs with cells and subsequent fluorescent imaging, we hereafter examine whether the μNDs would be suitable to probe individual cells via confocal fluorescence microscopy. Magnetic-only μNDs were previously found to be internalized by mouse fibroblasts and human cancer cells, a phenomenon which was used to extract viscoelastic properties of their cytoplasm through rotational magnetic spectroscopy.[13] Here, HeLa cells were incubated with QD-doped μNDs, fixed and stained with DAPI in order to fluorescently label their nucleus. It is worth noting that the μNDs were structurally stable in the culture medium over the duration of the incubation. **Figure 7** displays bright field (a, b) and fluorescence (c, d) confocal images acquired in two focal plans lying 6 μm apart selected from a stack of images acquired over a 10 μm depth. The blue and red fluorescence channels correspond to DAPI and QD emissions, respectively.

The $z = 6$ μm imaging plan was selected as it intersects the cells in the middle of the nuclei as evidenced by the neat contours of the cell membranes and of the nuclei in bright field (Figure 7b) and fluorescence (Figure 7d) images respectively. The $z = 0$ μm imaging plan intersects the cells on top or in the upper part of the nuclei. At both imaging heights, several dark objects of micrometric dimensions can be spotted in bright field mode (Figure 7a,b). Their outlines appear more clearly at $z = 6$ μm (Fig. 7b) and suggest they correspond to μNDs but their localizations with regards to the cellular compartments are difficult to assess. However in fluorescence

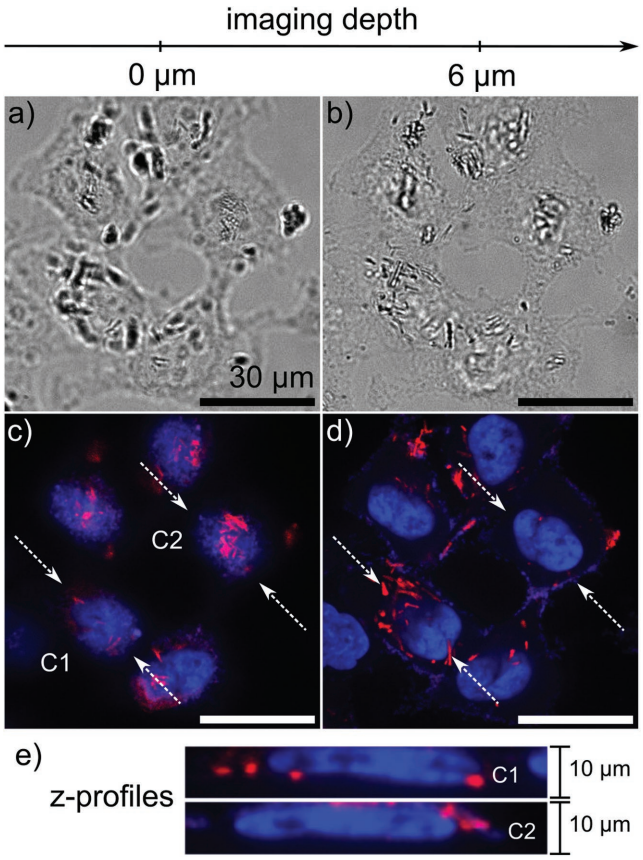

Figure 7. a,b) Bright field and c,d) fluorescent confocal images of HeLa cells incubated with bifunctional fluorescent magnetic μNDs (60X objective). e) Reconstructed *z*-profiles of cells **C1** and **C2** in the planes perpendicular to the highlighted directions of interest.

images at both imaging depths (Figure 7c,d), these objects appear as individual or entangled red needles or dashes with lengths comprised between 2 and 6 μm. Their shapes and dimensions indicate that they correspond to structurally intact μNDs that lie flat or tilted with regards to the imaging plan (see also Figure S20, Supporting Information). To examine the possibility of resolving their localizations, the fluorescence profile of two cells were reconstructed in two vertical planes passing through areas dense in μNDs (Figure 7e). The vertical plane attached to cell **C1** intersects four isolated μNDs which then appear in the reconstructed *z*-profile as bright red dots. These μNDs are located in (x,y) planes coinciding with the lower half of the nucleus, consistently with their displaying dim contrast at $z = 0$ μm and bright contrast at $z = 6$ μm. The positions of these μNDs with respect to the nucleus indicate that they are internalized by the cell but do not penetrate within the nuclear compartment. These μNDs could be selected as appropriate if one intended to mechanically probe the cytoplasm of the cell. Conversely, in the vertical plane attached to cell **C2**, entangled μNDs appear along the upper contour of the nucleus. Again, they are excluded from the nuclear compartment. These μNDs could either be sitting on top of the cell or on top of the nucleus within the cytoplasmic wall. The *z*-profile of cell **C2** does not disambiguate the situation as such but fluorescent labeling of the cell membrane would. Nevertheless, for the purpose of

probing the cytoplasm of the cell, these entangled μNDs should be discarded. At any rate, this example shows that like their magnetic-only counterparts, bifunctional μNDs can be internalized by mammalian cells but not by their nucleus. Moreover, it illustrates how the fluorescence feature of the μNDs may be used to quickly select those μNDs that are suitable in order to mechanically probe zones of rheological interest.

3. Conclusion

In this work, bifunctional microneedles were readily assembled by electrostatic complexation of a ternary mixture of superparamagnetic iron oxide nanoparticles, red-emitting $AgInS_2$-ZnS quantum dots and a cationic poylelectrolyte. The microneedles encompass the properties of both nanoparticle components, namely superparamagnetism and fluorescence in the visible range. They can be actuated using small external magnetic fields and imaged using epifluorescence or confocal fluorescence microscopy. Interestingly, we found that by playing on the ternary composition, more specifically on the ratio of negative charges brought by the nanoparticles to positive charges brought by the polyelectrolyte, the mean length of the microneedles can be tuned in the 5–50 μm range. Because of their easy synthesis, their bifunctionality and their size tunability, these fluorescent and magnetic microneedles could find applications in multiple domains such as micromixing, bioassays or biomechanical studies and especially in the field of cell mechanics, since we demonstrated that they can be internalized by model animal cells.

4. Experimental Section

Synthesis and Characterization of Nanoparticle Building Blocks: Maghemite mNPs were synthesized following the Massart procedure and surface-coated with sodium polyacrylate according to previously reported protocols.[32,33] PAA-coated ZAIS QDs were synthesized in one step following the method reported by Regulacio et al. with minor modifications.[31] Core material concentrations were determined by ICP-OES for QDs and X-ray fluorescence for mNPs. Concentrations of surface carboxylates were determined by pH-titration with HCl. The quantum yield of QDs was determined by comparison to those of fluorescein and rhodamine 6G.[46–48] Gel electrophoresis was performed on 1% wt agarose gel in TBE 1x buffer. A full description of the synthetic and characterization procedures is provided in Supporting Information.

Assembly of Fluorescent Magnetic Microneedles: The following gives the synthetic procedure for assembly of {$Z = 4.20$; $w = 0.20$} μNDs as an example. First, solutions of building blocks in NH_4Cl 1 M pH 8 were prepared by mixing in a 1:1 ratio an NH_4Cl 2 M pH 8 solution with the mNP (0.2% wt core, 2.02×10^{-3} M carboxylate), the QD (0.4% wt core, 14.73×10^{-3} M carboxylate), and polydiallyldimethylammonium chloride (0.2% wt, 13.4×10^{-3} M ammonium) stock solutions, respectively. Next, 400, 100, and 40.5 μL of mNP, QD and polymer dilute solutions were mixed in an Eppendorf tube and shaken for 10 s with the help of a vortex mixer. The ternary mixture was inserted in a 0.5–3 mL Slide-a-Lyzer dialysis cassette with a 10 kDa cutoff using a syringe. Air bubbles were removed. The cassette was nested into a custom made plexiglas sample holder sandwiched between two 5×8 cm^2 0.3 T magnets. The sample holder was then immersed in a 2.5 L cylindrical flask filled with deionized water equipped with a stir bar and continuous monitoring of the conductivity was launched immediately. Dialysis was run for 2 h after which the conductivity of the dialysis medium had reached a stable value. The content of the dialysis cassette had turned turbid, thereby evidencing successful assembly. The reaction media was carefully taken out using a syringe and inserted into a 2 mL glass vial. μNDs were sedimented using a soft table magnet and the supernatant was discarded. The μNDs were redispersed in 1 mL MilliQ water through gentle vortex mixing, sedimented again and the supernatant discarded. Two more washing steps using 2×1 mL MilliQ water were performed. Finally, the μNDs were redispersed in 1 mL MilliQ water and stored in the dark at 4 °C. The 14 other investigated compositions were prepared using the same protocol, with varying mNP, QD and polymer amounts, as given in Supporting Information. The microneedles were stable for at least two months stored in a fridge. Six months after synthesis, the larger and thicker microneedles were difficult to redisperse. Optical imaging revealed that they had irreversibly aggregated.

Imaging of μNDs using Phase Contrast and Epifluorescence Microscopy: A square well was built on a glass slide using double-sided tape. The μND suspension was homogenized and diluted four times with MilliQ water. 8 μL of this diluted suspension were deposited in the well, which was then covered with a coverslip. The sample was imaged in phase contrast mode and in epifluorescence mode using excitation and emission filters suited for Rhodamine 6G, with 10X, 20X, and 40X magnifications. Length and brightness distributions were extracted using custom-written Matlab codes (length extraction code can be downlloaded at http://lab513.github.io/HoughNeedles/).

Imaging of Fluorescent Magnetic μNDs in Interaction with HeLa Cells using Confocal Fluorescence Microscopy: **Preparation of μND sample.** For incubation of cells, we selected {$Z = 3.62$, $w = 0.15$} μNDs. This sample had a mean length amongst the shortest in all investigated compositions (15 μm). However, it was shown previously on a similar sized sample of magnetic-only μNDs that cells operate a size sorting of μNDs upon internalization, with an enrichment in μNDs having a length around 4 μm.[29] We therefore shortened the μNDs by ultrasonication before cell incubation. To this end, 400 μL were inserted in a 1 mm optical path quartz cuvette and sonicated for 2×1 min in an ultrasonic bath in horizontal position, with intermediate cooling for 5 min. The μNDs were sedimented in the cuvette using a table magnet and the supernatant was discarded. Next, they were washed three times with 500 μL MilliQ water through sedimentation and discarding of the supernatant. Finally, they were dispersed in 500 μL MilliQ water before autoclaving. **Cell culture.** HeLa cells were grown in T25-flasks as a monolayer in Dulbecco's Modified Eagle Medium (DMEM) with high glucose concentration (4.5 g L^{-1}) and stable glutamine (2×10^{-3} M, PAA Laboratories GmbH, Austria). This medium was supplemented with 10% vt fetal bovine serum and 1% penicillin/streptomycin (PAA Laboratories GmbH, Austria), referred to as cell culture medium. Exponentially growing cultures were maintained in a humidified atmosphere of 5% CO_2 and 95% air at 37 °C. In these conditions the plating efficiency was 70%–90% and the cell duplication time was 12–14 h. Cell cultures were passaged twice weekly using trypsin-EDTA to detach the cells from their culture flasks and wells. For counting, the cells were pelleted by centrifugation at 1200 rpm for 5 min, supernatants were removed and cell pellets were resuspended in assay medium in Malassez counting chambers. **Seeding of HeLa cells onto microscope glass coverslips.** Sterilized microscope coverslips were nested in the wells of a 6-well plate, washed with 1 mL of Phosphate Buffered Saline (PBS) and then with 1 mL of culture medium. Cells were detached from their culture flask and transferred to the wells; the cell concentration was 75 000 cells mL^{-1} and each well contained 2 mL of cell suspension. The cells were incubated for 24 h to promote cell adhesion onto the coverslips. **Incubation of HeLa cells with μNDs.** The cell medium was exchanged against 2 mL of PBS buffer and exchanged again for 1 mL of culture medium. Next, 15, 30, or 40 μL of shortened μNDs were mixed with 1 mL of culture medium and the resulting suspension was added dropwise in each well. The cells were incubated with the μNDs for 20 h after which they were washed by two rounds of medium exchange against PBS buffer. **Cell fixation.** Next, the cells were fixed through incubation in 4% PFA solution (J61899, Alfa Aesar) in PBS for 20 min at room temperature. After copious rinsing of

PFA using PBS, the nuclei were fluorescently stained with 4′,6-diamidino-2-phenylindole dilactate dye (DAPI dilactate, 98%, Aldrich) by incubation for 20 min at room temperature in a 2.2×10^{-6} M dye solution in PBS. The medium was exchanged for PBS three times to remove excess dye. Finally, microscope slides were equipped with Gene Frame stickers. The coverslips were carefully taken out of the wells and mounted onto the Gene Frames after filling the wells with PBS buffer. Samples were examined with an inverted wide-field microscope (Olympus IX81) equipped with spinning disc module (Yokogawa CSU-X1), with an oil immersion objective (60X, NA 1.42) and an EMCCD camera (Andor iXon 897). *Z*-stacks of wide-field fluorescent images were acquired using a piezo at 0.5 µm increments. For the DAPI channel, 405 nm laser-line excitation and a 465 nm centered emission filter were used. For the µND channel, the excitation line was 488 nm and the emission filter was centered at 607 nm.

Supporting Information

Supporting Information is available from the Wiley Online Library or from the author.

Acknowledgements

G.C. thanks J.-M. Di Meglio for his critical reading of the manuscript.

Conflict of Interest

The authors declare no conflict of interest.

Keywords

1D-microstructures, fluorescence imaging, magnetic nanoparticles, nanoparticle assembly, quantum dots

Received: January 20, 2017
Revised: March 31, 2017
Published online:

[1] R. M. Erb, R. Libanori, N. Rothfuchs, A. R. Studart, *Science* **2012**, *335*, 199.
[2] K. Ward, Z. H. Fan, *J. Micromech. Microeng.* **2015**, *25*, 094001.
[3] W. H. Chong, L. K. Chin, R. L. S. Tan, H. Wang, A. Q. Liu, H. Chen, *Angew. Chem. Int. Ed.* **2013**, *52*, 8570.
[4] D. D. Bruyker, M. I. Recht, A. A. S. Bhagat, F. E. Torres, A. G. Bell, R. H. Bruce, *Lab Chip* **2011**, *11*, 3313.
[5] K. S. Ryu, K. Shaikh, E. Goluch, Z. Fan, C. Liu, *Lab Chip* **2004**, *4*, 608.
[6] S. L. Biswal, A. P. Gast, *Anal. Chem.* **2004**, *76*, 6448.
[7] H. Yu, T.-B. Nguyen, S. H. Ng, T. Tran, *RSC Adv.* **2016**, *6*, 11822.
[8] A. Alfadhel, J. Kosel, *Adv. Mater.* **2015**, *27*, 7888.
[9] A. Alfadhel, B. Li, A. Zaher, O. Yassine, J. Kosel, *Lab Chip* **2014**, *14*, 4362.
[10] Y. Gao, B. Zhou, X. Wu, X. Gao, X. Zeng, J. Xie, C. Wang, Z. Ye, J. Wan, W. Wen, *ACS Biomater. Sci. Eng.* **2016**, *2*, 65.
[11] J. le Digabel, N. Biais, J. Fresnais, J.-F. Berret, P. Hersen, B. Ladoux, *Lab Chip* **2011**, *11*, 2630.
[12] N. J. Sniadecki, C. M. Lamb, Y. Liu, C. S. Chen, D. H. Reich, *Rev. Sci. Instrum.* **2008**, *79*, 044302.
[13] J.-F. Berret, *Nat. Commun.* **2016**, *7*, 10134.
[14] L. Chevry, N. K. Sampathkumar, A. Cebers, J.-F. Berret, *Phys. Rev. E* **2013**, *88*, 062306.
[15] D. Wirtz, *Annu. Rev. Biophys.* **2009**, *38*, 301.
[16] T. A. Waigh, *Rep. Prog. Phys.* **2005**, *68*, 685.
[17] H. Labiadh, T. Ben Chaabane, R. Sibille, L. Balan, R. Schneider, *Beilstein J. Nanotechnol.* **2015**, *6*, 1743.
[18] P. Jing, Q. Wang, B. Liu, G. Xu, Y. Zhang, J. Zhang, G. De, *RSC Adv.* **2014**, *4*, 44575.
[19] Y. Lu, Y. Zheng, S. You, F. Wang, Z. Gao, J. Shen, W. Yang, M. Yin, *ACS Appl. Mater. Interfaces* **2015**, *7*, 5226.
[20] N. Hassan, V. Cabuil, A. Abou-Hassan, *Angew. Chem. Int. Ed.* **2013**, *52*, 1994.
[21] J. Peng, L.-N. Feng, K. Zhang, J.-J. Li, L.-P. Jiang, J.-J. Zhu, *Chem. – Eur. J.* **2011**, *17*, 10916.
[22] T. Bollhorst, S. Shahabi, K. Wörz, C. Petters, R. Dringen, M. Maas, K. Rezwan, *Angew. Chem. Int. Ed.* **2015**, *54*, 118.
[23] X. Sun, K. Ding, Y. Hou, Z. Gao, W. Yang, L. Jing, M. Gao, *J. Phys. Chem. C* **2013**, *117*, 21014.
[24] R. Di Corato, N. C. Bigall, A. Ragusa, D. Dorfs, A. Genovese, R. Marotta, L. Manna, T. Pellegrino, *ACS Nano* **2011**, *5*, 1109.
[25] H. Wang, J. Yi, S. Mukherjee, P. Banerjee, S. Zhou, *Nanoscale* **2014**, *6*, 13001.
[26] B. K. Gupta, S. Singh, P. Kumar, Y. Lee, G. Kedawat, T. N. Narayanan, S. A. Vithayathil, L. Ge, X. Zhan, S. Gupta, A. A. Martí, R. Vajtai, P. M. Ajayan, B. A. Kaipparettu, *Sci. Rep.* **2016**, *6*, 32401.
[27] J. Fresnais, J.-F. Berret, B. Frka-Petesic, O. Sandre, R. Perzynski, *Adv. Mater.* **2008**, *20*, 3877.
[28] M. Yan, J. Fresnais, J.-F. Berret, *Soft Matter* **2010**, *6*, 1997.
[29] M. Safi, M. Yan, M.-A. Guedeau-Boudeville, H. Conjeaud, V. Garnier-Thibaud, N. Boggetto, A. Baeza-Squiban, F. Niedergang, D. Averbeck, J.-F. Berret, *ACS Nano* **2011**, *5*, 5354.
[30] M. Yan, J. Fresnais, S. Sekar, J.-P. Chapel, J.-F. Berret, *ACS Appl. Mater. Interfaces* **2011**, *3*, 1049.
[31] M. D. Regulacio, K. Y. Win, S. L. Lo, S.-Y. Zhang, X. Zhang, S. Wang, M.-Y. Han, Y. Zheng, *Nanoscale* **2013**, *5*, 2322.
[32] R. Massart, E. Dubois, V. Cabuil, E. Hasmonay, *J. Magn. Magn. Mater.* **1995**, *149*, 1.
[33] L. Qi, J.-P. Chapel, J.-C. Castaing, J. Fresnais, J.-F. Berret, *Langmuir* **2007**, *23*, 11996.
[34] P. Subramaniam, S. J. Lee, S. Shah, S. Patel, V. Starovoytov, K.-B. Lee, *Adv. Mater.* **2012**, *24*, 4014.
[35] G. Charron, D. Hühn, A. Perrier, L. Cordier, C. J. Pickett, T. Nann, W. J. Parak, *Langmuir* **2012**, *28*, 15141.
[36] R. O. Duda, P. E. Hart, *Commun. ACM* **1972**, *15*, 11.
[37] W. Liu, J. Mao, Y. Xue, Z. Zhao, H. Zhang, X. Ji, *Langmuir* **2016**, *32*, 7596.
[38] J. A. Flores, A. A. Jahnke, A. Pavia-Sanders, Z. Cheng, K. L. Wooley, *Soft Matter* **2016**, *12*, 9342.
[39] T. Bollhorst, T. Grieb, A. Rosenauer, G. Fuller, M. Maas, K. Rezwan, *Chem. Mater.* **2013**, *25*, 3464.
[40] V. Lobaz, R. N. Klupp Taylor, W. Peukert, *J. Colloid Interface Sci.* **2012**, *374*, 102.
[41] K. L. Thompson, S. P. Armes, D. W. York, *Langmuir* **2011**, *27*, 2357.
[42] R. Di Corato, P. Piacenza, M. Musarò, R. Buonsanti, P. D. Cozzoli, M. Zambianchi, G. Barbarella, R. Cingolani, L. Manna, T. Pellegrino, *Macromol. Biosci.* **2009**, *9*, 952.
[43] I. Sinn, T. Albertson, P. Kinnunen, D. N. Breslauer, B. H. McNaughton, M. A. Burns, R. Kopelman, *Anal. Chem.* **2012**, *84*, 5250.
[44] V. Swaminathan, K. Mythreye, E. T. O'Brien, A. Berchuck, G. C. Blobe, R. Superfine, *Cancer Res.* **2011**, *71*, 5075.
[45] T. Grevesse, B. E. Dabiri, K. K. Parker, S. Gabriele, *Sci. Rep.* **2015**, *5*, 9475.
[46] A. M. Brouwer, *Pure Appl. Chem.* **2011**, *83*, 2213.
[47] M. Fischer, J. Georges, *Chem. Phys. Lett.* **1996**, *260*, 115.
[48] L. Porrès, A. Holland, L.-O. Pålsson, A. P. Monkman, C. Kemp, A. Beeby, *J. Fluoresc.* **2006**, *16*, 267.

